

## THE ORBITAL NATURE OF 81 ELLIPSOIDAL RED GIANT BINARIES IN THE LARGE MAGELLANIC CLOUD

J. D. NIE<sup>1</sup>, P. R. WOOD<sup>2</sup>, C. P. NICHOLLS<sup>3</sup>

*Published 2017 January 31, The Astrophysical Journal, Volume 835, Number 2*

### ABSTRACT

In this paper, we collect a sample of 81 ellipsoidal red giant binaries in the LMC and we study their orbital natures individually and statistically. The sample contains 59 systems with circular orbits and 22 systems with eccentric orbits. We derive orbital solutions using the 2010 version of the Wilson–Devinney code. The sample is selection-bias corrected and the orbital parameter distributions are compared to model predictions for the LMC and to observations in the solar vicinity. The masses of the red giant primaries are found to range from about 0.6–9  $M_{\odot}$  with a peak at around 1.5  $M_{\odot}$ , in agreement with studies of the star formation history of the LMC which find a burst of star formation beginning around 4 Gyr ago. The observed distribution of mass ratios  $q = m_2/m_1$  is more consistent with the flat  $q$  distribution derived for the solar vicinity by Raghavan et al. (2010) than it is with the solar vicinity  $q$  distribution derived by Duquennoy & Mayor (1991). There is no evidence for an excess number of systems with equal mass components. We find that about 20% of the ellipsoidal binaries have eccentric orbits, twice the fraction estimated by Soszynski et al. (2004). Our eccentricity evolution test shows that the existence of eccentric ellipsoidal red giant binaries on the upper parts of the red giant branch (RGB) can only be explained if tidal circularization rates are  $\sim 1/100$  the rates given by the usual theory of tidal dissipation in convective stars.

*Subject headings:* stars: AGB and post-AGB – binaries: close – Magellanic Clouds

### 1. INTRODUCTION

Ellipsoidal red giant binaries are close binary systems consisting of a distorted red giant and, in most cases, an unseen companion. The red giant is distorted into a roughly ellipsoidal shape because it fills a large fraction of its Roche lobe. Orbital rotation of the distorted red giant gives rise to a characteristic change in apparent brightness, with two light maxima and two light minima in each orbital period in contrast to the radial velocity variation which has one maximum and one minimum per orbit (e.g. Morris 1985; Nicholls et al. 2010; Nie & Wood 2014).

The ellipsoidal red giant binaries in the Large Magellanic Cloud (LMC) are also known as sequence E stars because of another characteristic property – these stars lie on a distinct linear Period–Luminosity (PL) sequence named sequence E (Wood et al. 1999; Soszynski et al. 2004). The position of this sequence in the PL plane can vary between different publications depending on whether the period adopted is the orbital period or the period between light maxima (e.g. Wood 2000; Ita et al. 2004; Soszynski et al. 2007; Fraser et al. 2008). The orbital periods of sequence E stars from the above papers lie in the range  $\sim 40$ –1000 days while apparent  $K$  magnitudes lie in the range  $\sim 12$ –16 although fainter and shorter-period ellipsoidal variables do exist on the red giant branch in the LMC (Pawlak et al. 2014).

The PL sequence is basically a sequence of binary systems born with different separations. A red giant almost fills its Roche lobe in an ellipsoidal binary system and the orbital separation of the two stars is typically 3–4 times the radius of the red giant. A larger orbital separation thus requires a larger

radius  $R$  and hence a higher luminosity  $L$  for the red giant. Since a larger separation also leads to a larger orbital period via Kepler’s third law, a PL sequence for ellipsoidal red giant binaries results (e.g. see Figure 4 of Wood et al. 1999, where the observed period used for the sequence E stars is the time between light maxima (the photometric period), which is half the orbital period). Mass variations of the components of the binary and variations in the Roche lobe filling factor both lead to a scatter in the PL relation (Soszynski et al. 2004).

In ellipsoidal red giant binaries, the red giant is an AGB or RGB star undergoing radius expansion as it evolves and the red giant is about to fill its Roche lobe. At the same time, the unseen companion, which is usually a main sequence star of lower mass, keeps its size and luminosity relatively small and unchanged. When the red giant fills its Roche lobe, the companion gains mass from the donor red giant, usually in a run-away process, and this kind of dynamical mass transfer builds up a common envelope around the two bodies. The common envelope event quickly creates a close binary planetary nebula (PN), a binary post–AGB star, a binary post–RGB star or a merged star that will continue to evolve as a red giant (Nie et al. 2012). An alternative stable mass transfer process on an evolutionary timescale can occur for a small range in the mass ratio of the two stars in the binary system (e.g. Han et al. 2002).

In order to make population formation studies of the descendants of the interacting binary systems mentioned above, a knowledge of the orbital properties and frequency of occurrence of their parent systems is essential. Since the ellipsoidal red giant binaries are the immediate precursor binaries of above descendants, a knowledge of their orbital properties in the population under study should put strict constraints on binary population simulation models. In particular, we need to know properties such as the statistical distributions of the binary masses  $m_1$  and  $m_2$ , the mass ratio  $q = m_2/m_1$ , the orbital separation  $a$  and the eccentricity  $e$ . All these properties can be obtained for ellipsoidal red giant binaries provided

<sup>1</sup> Key Laboratory of Optical Astronomy, National Astronomical Observatories, Chinese Academy of Sciences, Beijing 100012, China; jdnie@bao.ac.cn

<sup>2</sup> Research School of Astronomy and Astrophysics, Australian National University, Canberra, ACT 2611, Australia; peter.wood@anu.edu.au

<sup>3</sup> Institute for Astrophysics, University of Vienna, Türkenschanzstraße 17, 1180 Wien, Austria; christine.nicholls@univie.ac.at

light and velocity curves exist.

The LMC is an ideal stellar population to study because, in addition to a well-determined population of ellipsoidal red giant binaries (from the MACHO and OGLE II microlensing experiments), there exist quite well known populations of many other stellar types such as RGB stars, AGB stars, post-RGB stars, post-AGB stars and planetary nebulae. Thus the populations predicted by binary population modelling can be compared to the observed population. Such modelling was done by Nie et al. (2012) but they adopted orbital element distributions from the solar vicinity studies of Duquennoy & Mayor (1991) and Raghavan et al. (2010). It is desirable to see if the same distributions exist in samples of binaries in the LMC where there is a different metallicity distribution and a different star formation history. The LMC ellipsoidal red giant variable population therefore provides an opportunity to directly determine orbital element distributions in LMC binary systems. This is the aim of this paper.

To determine the complete orbital properties of ellipsoidal red giant binaries at a known distance (which is the case for LMC binaries), light curves and radial velocity data are sufficient (see subsection 3.2 of this paper for a justification). Examples of the derivation of complete orbital parameters for ellipsoidal variables at a known distance are given in Wilson et al. (2009) and Nicholls & Wood (2012). Thanks to the MACHO and OGLE projects, extensive light curve data are available for LMC ellipsoidal red giant binaries, along with good estimates of the populations of these systems. However, radial velocity data are rare because it is very time consuming to cover even one orbit given the long orbital periods and only a few radial velocity studies have been carried out up to now. Nicholls et al. (2010) took radial velocity observations of 11 ellipsoidal variables in the LMC and roughly estimated orbital parameters for the systems. However, for a complete understanding of those objects, a more accurate parameter determination is needed. As a special study of the ellipsoidal binaries, Nicholls & Wood (2012) monitored radial velocities for 7 highly eccentric systems in the LMC and determined their orbital parameters with the 2010 version of the Wilson–Devinney (hereinafter WD) code (Wilson & Devinney 1971; Wilson 1979, 1990; Wilson et al. 2009), which can produce complete orbital solutions if the absolute luminosity is known, as it is for stars in the LMC. That paper is the only existing work that gives complete solutions for LMC ellipsoidal variables.

In order to have larger samples, and to select objects with as wide a set of parameters as possible, Nie & Wood (2014) carried out radial velocity observations of 80 ellipsoidal red giant binaries in the LMC. They provided radial velocity curves for individual stars as well as some statistics on the observed stellar parameters. However, orbital parameters were not determined for these binaries and this is the main goal of this paper. We use the 2010 version of the WD code to attempt modelling of 79 ellipsoidal variables in Nie & Wood (2014). In addition, we attempt modelling of the 11 objects in Nicholls et al. (2010) in order to better determine their orbital parameters. Together with the 7 eccentric systems in Nicholls & Wood (2012) whose orbital solutions we also attempt to re-derive using the methods in this paper for consistency, we have an initial sample of 97 ellipsoidal binaries. (We only modelled 79 of the 80 objects in Nie & Wood (2014) as one object had already been observed by Nicholls & Wood (2012).) The complete sample can provide us with statistical information about the properties of LMC binaries with intermediate initial sep-

arations such that binary interactions occur on the RGB or AGB. These properties can be compared to the properties of similar binaries in the solar vicinity. In addition, by comparing the observed binary properties with binary evolution models, we can investigate the assumptions of the evolution models such as the effect of tides on eccentricity evolution.

## 2. OBSERVATIONAL DATA

In order to model the orbits of the LMC ellipsoidal variables, we require both light and velocity curves. The light curve data we use are mainly from OGLE II (Szymanski 2005; Udalski et al. 1997; Soszynski et al. 2004), sometimes supplemented by OGLE III data if it is published. The light curves are in the  $I$  band. The radial velocities are provided by Nie & Wood (2014) for 79 ellipsoidal variables, by Nicholls et al. (2010) for their 11 ellipsoidal variables and by Nicholls & Wood (2012) for their 7 eccentric binaries. The light curve photometry, supplemented by  $K$ -band photometry from the Two Micron All Sky Survey (2MASS) catalog (Cutri et al. 2003), provides the  $K$  magnitude and the  $I - K$  color. From these and the adopted LMC distance modulus of 18.49 (de Grijs et al. 2014) and reddening  $E(B-V) = 0.08$  (Keller & Wood 2006), the basic stellar parameters effective temperature  $T_{\text{eff1}}$ , luminosity  $L_1$ , and the mean radius  $R_1$  of the primary star can be computed (see Nie & Wood 2014 for the details of the calculation of these quantities). The light and velocity curve data also allow derivation of the orbital period  $P$  and the radial velocity semi-amplitude  $K_1$  of the red giant.

## 3. MODELLING DETAILS

In order to get a converged solution in the WD code, a reasonably accurate approximation to the final solution is required as input. This is especially so when a large number of solutions is sought as is the case here. Hence, we used a separate code to estimate the initial orbital parameters. This code uses the equations below to determine an approximate solution that is fed into the WD code for iterative refinement. The eccentricity is assumed to be zero. Firstly, we have Kepler's Law

$$\frac{m_1(1+q)}{a^3} = \frac{4\pi^2}{GP^2} \quad (1)$$

where  $m_1$  is the mass of the red giant,  $q$  is the mass ratio  $m_2/m_1$ ,  $m_2$  is the mass of the unseen companion,  $a$  is the semi-major axis of the orbit, and  $G$  is the gravitational constant. Secondly, we have the equation for the binary mass function

$$\frac{m_1 q^3 \sin^3 i}{(1+q)^2} = \frac{K_1^3 P}{2\pi G}, \quad (2)$$

where  $K_1$  is radial velocity semi-amplitude of the red giant and  $i$  is the angle of inclination of the orbit. Next we use the relation between the light variation amplitude and the mass ratio for ellipsoidal variables given in Nie et al. (2012)

$$\frac{\Delta I}{0.87 \sin^2 i} = (0.221f^4 + 0.005)(1.44956q^{0.25} - 0.44956), \quad (3)$$

where  $\Delta I$  is the full light curve amplitude in the  $I$  band and  $f$  is the Roche lobe filling factor given by

$$f = \frac{R_1}{R_L}. \quad (4)$$

Here,  $R_L$  is the effective Roche lobe radius (Eggleton 1983) given by

$$\frac{R_L}{a} = \frac{0.49q^{-2/3}}{0.6q^{-2/3} + \ln(1 + q^{-1/3})}, \quad 0 < q < \infty. \quad (5)$$

The quantities  $P$ ,  $K_1$ ,  $\Delta I$  and  $R_1$  are known from observations of the light/velocity curves and from 2MASS photometry, and we assume various values for the orbital inclination  $i$  (see below). In this situation, the five equations above can be solved iteratively for the five unknown variables  $m_1$ ,  $q$ ,  $a$ ,  $f$  and  $R_L$  given that  $i$  is prescribed.

As well as the above parameters, the WD code requires other input. The systematic velocity  $V_\gamma$  is determined by fitting the velocity curve. The zero-point of the orbital ephemeris  $HJD_0$ , which corresponds to the light minimum where the radial velocity is becoming more negative (superior conjunction), is obtained by fitting the  $I$  band light curve to find the times of the two light minima then selecting the one where the velocity curve is decreasing. The final object-related parameters that the WD code requires as input are the effective temperatures  $T_{\text{eff}1}$  and  $T_{\text{eff}2}$  of the red giant and companion, respectively, and the dimensionless surface potentials  $\Omega_1$  and  $\Omega_2$  of these stars (the WD code iterates to the best solution value of  $\Omega_1$  but an input guess is required). As noted above,  $T_{\text{eff}1}$  is obtained from photometry while  $\Omega_1$  is approximated by the potential at outer end of star 1 along the line of centres where

$$\Omega_1 = \frac{1}{\rho_1} + q\left(\frac{1}{1 + \rho_1} + \rho_1\right) + \frac{1}{2}(1 + q)\rho_1^2 \quad (6)$$

and  $\rho_1 = R_1/a$ . The red giant radius  $R_1$  is obtained from  $T_{\text{eff}1}$  and the observed luminosity  $L_1$  using the equation

$$L_1 = 4\pi\sigma R_1^2 T_{\text{eff}1}^4. \quad (7)$$

To get the parameters for the secondary star, we assume that it lies in the middle of the main sequence. The evolutionary tracks of Bertelli et al. (2008) for an LMC metallicity of  $Z = 0.008$  and masses between 0.8 and 8  $M_\odot$  were approximated at this phase of evolution to yield the equations

$$T_{\text{eff}2} = 6072\left(\frac{m_2}{M_\odot}\right)^{0.599} \quad (8)$$

and

$$\frac{R_2}{R_\odot} = 1.16\left(\frac{m_2}{M_\odot}\right)^{0.756} \quad (9)$$

where  $R_2$  is the radius of the companion star. The dimensionless surface potential  $\Omega_2$  for the companion was then computed using the equation

$$\Omega_2 = \frac{1}{\rho_2} + q_2\left(\frac{1}{1 + \rho_2} + \rho_2\right) + \frac{1}{2}(1 + q_2)\rho_2^2 \quad (10)$$

where  $q_2 = 1/q$  and  $\rho_2 = R_2/a$ . Note that  $L_2$  is not an input parameter to the WD code but it is calculated using the analog of Equation 7. Provided the companion star is much less luminous than the red giant and of small size compared to the red giant Roche lobe radius, then the actual values of  $T_{\text{eff}2}$  and  $\Omega_2$  do not affect the orbital solution significantly. In nearly all our objects, the companion is indeed very faint compared to the red giant as it is not seen in either the photometry or the spectra. The companion is therefore most likely a main sequence star or a compact star (white dwarf or neutron star). However, we found no emission lines characteristic of

an accreting white dwarf or neutron star companion in any of our spectra so main sequence star companions are most likely (Nie & Wood 2014).

### 3.1. Creating an $i$ - $q$ relation

We are now in a position to use the WD code to create an  $i$ - $q$  relation for the system under study. The WD code is composed of two main programs: DC and LC. The DC program uses differential corrections to calculate the orbital parameters and LC uses the converged solutions from DC to calculate stellar masses and fit the light and velocity curves. The basic procedure is: for a circular orbit binary system, we set  $HJD_0$ ,  $V_\gamma$ ,  $P$ ,  $T_{\text{eff}1}$ ,  $T_{\text{eff}2}$ ,  $\Omega_1$  and  $\Omega_2$  with initial values derived as described above, as well as setting  $i = 90$  degrees and  $e = 0$ . The DC code is then set to iterate on  $HJD_0$ ,  $V_\gamma$ ,  $a$ ,  $\Omega_1$  and  $q$ . Then we step the input value of  $i$  down from 90 degrees, in 5 degree increments to produce a one-dimensional family of solutions (an  $i$ - $q$  sequence) for each system. The solutions are found using mode 2 for the ellipsoidal binaries, which are detached systems. A simple reflection treatment is used, with no spots, no proximity effects and no third body in the system. The stars are assumed to have their rotation velocities synchronized at periastron. The gravity brightening exponent of the bolometric gravity brightening law for the red giant,  $g_1$ , is set to the value given by the non-grey version of Equation 2 in Alencar & Vaz (1997) who evaluated  $g_1$  from convective stellar atmosphere models. For our typical red giants with  $T_{\text{eff}1} \sim 4000$  K,  $g_1 \approx 0.3$ . For the main sequence companion, we set  $g_2 = 1.0$  as appropriate for a radiative envelope, although in practice the value of  $g_2$  is unimportant due to the relatively low luminosity of the companion to the red giant. Bolometric albedos for reflection heating and re-radiation are set to  $A_1 = 0.5$  for the red giant and  $A_2 = 1.0$  for the companion, again as expected for convective and radiative envelopes. Limb darkening is treated using the bolometric square root law, with the coefficients determined locally in the DC code.

In general, DC solutions converged (corrections  $\ll$  errors) in six to eight iterations when  $i$  was set. Stepping of  $i$  was stopped at 30 degrees, or when the solution was deemed to be getting too poor. Solutions with either companion exceeding its critical Roche lobe radius were rejected. For eccentric systems, a similar approach was applied but DC was allowed to adjust two extra parameters, the eccentricity  $e$  and the argument of periastron for the red giant,  $\omega$ .

### 3.2. Finding the best solution from the $i$ - $q$ relation

Morris (1985) showed that the time variation of the light curves of ellipsoidal variables could be approximated by the sum of terms proportional to  $\cos(\phi)$ ,  $\cos(2\phi)$  and  $\cos(3\phi)$  where  $\phi$  is the orbital phase. The coefficients of these terms depend on the orbital parameters  $q$ ,  $\sin(i)$  and  $R_1/a$  as well as on gravity brightening and limb darkening. The dominant  $\cos(2\phi)$  term gives rise to the characteristic light curve shape with two cycles of the light curve per orbital period and this term essentially determines the total amplitude of the ellipsoidal light variation. Adjusting the orbital parameters to fit the  $\cos(2\phi)$  term to the light curve is equivalent to defining Equation 3. As seen above, such fitting of the total amplitude of light variation is sufficient to give an initial guess for the orbital parameters of ellipsoidal variables when  $i$  is pre-defined. However, further information is required to estimate  $i$  as well as the other orbital parameters. This information comes largely from the  $\cos(3\phi)$  term.





TABLE 1 (continued)

Object	$P$	$T_{\text{eff1}}$	$HJD_0$	$V_\gamma$	$i$	$a$	$e$	$\omega$	$q$	$\Omega_1$	$m_1$	$m_2$	$R_1$	$R_{L,1}$	$R_2$	$L_1$	$L_2$
OGLE II	(day)	(K)	(2450000.0+)	(km s $^{-1}$ )	(deg)	(R $_G$ )		(rad)			(M $_G$ )	(M $_G$ )	(R $_G$ )	(R $_G$ )	(R $_G$ )	(L $_G$ )	(L $_G$ )
053946.88-704257.8	265.0	3929	5987.2±0.7	227.6±0.3	67.0±43.8	234.3±5.9	0.000	-	0.979±0.638	5.613±0.691	1.24±0.41	1.22±0.41	50.9	89.2	2.9	500.7	5.3
054258.34-701609.2	164.0	4114	5578.8±0.9	298.5±0.2	90.0	177.1±6.5	0.000	-	0.223±0.011	3.601±0.114	2.27±0.25	0.51±0.06	53.0	90.6	0.4	696.9	0.1
054736.16-705627.2	135.9	4244	5624.8±0.3	277.9±0.2	84.2±9.0	188.0±5.0	0.000	-	0.334±0.016	4.297±0.093	3.62±0.29	1.21±0.11	47.8	89.5	1.2	671.3	2.5
<b>Circular orbits (Nicholls et al. (2010))</b>																	
052613.43-694448.2	110.5	4027	5595.1±0.1	281.6±0.2	90.0	143.7±0.7	0.000	-	0.687±0.009	3.602±0.020	1.94±0.03	1.33±0.02	50.6	59.2	1.4	567.4	4.9
052656.70-695204.0	442.7	4046	5609.3±1.7	247.5±0.5	90.0	293.3±7.9	0.000	-	0.301±0.024	3.503±0.105	1.33±0.11	0.40±0.04	92.9	142.3	0.4	1963.9	0.0
052740.75-693539.5	131.4	4407	5639.1±0.1	252.1±0.1	80.5±5.9	139.2±0.5	0.000	-	0.832±0.029	4.117±0.033	1.15±0.02	0.95±0.02	43.2	55.0	1.0	663.5	1.3
052805.59-694732.8	139.2	4194	5603.6±0.1	350.8±0.1	71.7±4.6	153.3±0.7	0.000	-	0.680±0.034	3.644±0.036	1.49±0.04	1.01±0.03	53.0	63.2	1.0	773.7	1.4
052808.39-695504.9	157.7	3973	5659.0±0.2	255.2±0.2	90.0	141.3±0.7	0.000	-	0.418±0.007	2.972±0.018	1.08±0.02	0.45±0.01	57.2	64.4	0.4	675.0	0.0
052837.68-695250.9	327.4	3806	5793.3±0.6	275.0±0.4	74.0±14.5	291.2±5.2	0.000	-	0.539±0.074	3.534±0.081	2.01±0.15	1.08±0.11	99.3	126.2	1.1	1569.8	1.7
052852.69-694933.6	128.8	4304	5603.5±0.2	231.1±0.1	71.0±9.2	139.6±1.4	0.000	-	0.396±0.035	3.436±0.028	1.58±0.06	0.62±0.04	46.7	64.3	0.6	689.5	0.1
052853.08-695557.9	191.5	4332	5609.1±0.3	238.2±0.2	40.9±2.9	231.0±1.5	0.000	-	1.058±0.130	4.339±0.154	2.19±0.15	2.32±0.15	72.0	86.4	0.0	1694.2	0.0
052913.51-695632.3	65.7	4804	5580.0±0.1	255.0±0.3	69.4±0.5	134.9±0.7	0.000	-	0.778±0.014	3.730±0.023	4.30±0.08	3.35±0.06	47.0	54.1	2.6	1169.6	230.2
052917.67-694137.9	282.5	3918	5673.5±0.4	305.1±0.2	75.5±9.9	228.2±1.6	0.000	-	0.681±0.056	3.874±0.064	1.19±0.05	0.81±0.04	72.9	94.1	0.8	1010.6	0.5
<b>eccentric orbits (Nie &amp; Wood (2014))</b>																	
050610.03-683153.0	318.5	4197	5766.7±1.3	279.3±0.3	61.8±16.2	278.0±9.0	0.202±0.018	0.327±0.124	0.830±0.229	6.242±0.350	1.56±0.25	1.29±0.23	53.7	109.9	1.6	795.3	5.1
051009.20-690020.0	321.3	4023	5997.8±0.0	292.1±0.4	74.3±22.6	264.0±10.0	0.090±0.021	2.191±0.186	0.299±0.055	4.225±0.113	1.84±0.22	0.55±0.10	68.5	128.2	0.5	1035.0	0.1
051101.04-691425.1	282.5	4173	5809.2±2.0	212.7±0.6	55.9±4.7	217.9±7.5	0.254±0.022	6.432±0.108	0.416±0.053	4.814±0.179	1.23±0.13	0.51±0.07	52.3	99.4	0.5	730.9	0.1
051200.23-690838.4	641.3	3737	6504.3±2.8	245.6±0.4	90.0	455.3±12.5	0.278±0.013	3.824±0.068	0.237±0.017	3.637±0.109	2.49±0.21	0.59±0.06	139.3	230.4	0.5	2730.9	0.1
051220.63-684957.8	486.5	3983	5944.3±1.9	308.7±0.4	90.0	338.1±7.0	0.061±0.014	6.267±0.218	0.379±0.023	3.798±0.089	1.59±0.10	0.60±0.05	100.9	157.1	0.5	2127.2	0.1
051347.73-693049.7	306.6	4114	5773.3±1.2	252.5±0.3	36.1±3.4	214.8±4.4	0.138±0.020	4.578±0.113	0.837±0.143	4.721±0.190	0.77±0.08	0.65±0.07	58.7	84.7	0.6	856.2	0.2
051738.19-694848.4	297.7	3943	5882.7±1.3	238.5±0.3	74.5±15.3	275.5±6.3	0.353±0.017	5.354±0.060	0.443±0.017	4.744±0.126	2.20±0.17	0.97±0.11	68.4	124.2	0.9	923.3	1.0
051818.84-690751.3	463.9	3710	6119.3±1.3	264.0±0.2	90.0	336.5±5.8	0.195±0.014	4.655±0.075	0.528±0.021	4.753±0.073	1.56±0.08	0.82±0.05	82.8	146.4	0.8	909.1	0.4
052542.11-694847.4	514.6	4004	5703.5±1.9	263.8±0.7	54.5±1.5	473.9±12.1	0.267±0.008	1.006±0.049	0.696±0.053	5.553±0.156	3.18±0.23	2.22±0.17	105.1	194.6	2.0	2375.3	40.5
052948.84-692318.7	421.7	3872	6177.0±1.1	246.9±0.3	36.4±1.5	264.6±5.4	0.126±0.011	4.729±0.069	0.718±0.067	3.921±0.111	0.82±0.06	0.59±0.05	89.1	107.9	0.6	1414.4	0.1
053141.27-700647.1	384.1	3751	5852.1±0.8	215.1±0.5	55.7±2.6	311.0±6.3	0.054±0.006	1.032±0.128	0.540±0.044	3.458±0.090	1.78±0.12	0.96±0.08	111.1	134.7	0.9	1783.5	0.9
053156.08-693123.0	412.2	3916	5959.7±0.9	252.8±0.3	42.2±2.0	303.6±4.8	0.069±0.008	2.972±0.098	0.821±0.071	4.149±0.110	1.21±0.07	1.00±0.07	95.5	120.2	1.1	1733.6	1.7
053202.44-693209.2	426.5	4042	5792.9±1.7	234.6±1.2	90.0	285.7±12.1	0.078±0.012	7.142±0.158	0.595±0.075	5.279±0.274	1.08±0.15	0.64±0.10	62.0	121.3	0.6	870.0	0.1
053226.48-700604.7	454.0	3817	5899.7±1.5	276.2±0.4	79.4±6.1	365.8±5.9	0.221±0.012	5.556±0.058	0.862±0.053	5.139±0.106	1.71±0.10	1.48±0.09	93.3	143.3	1.8	1410.7	8.7
054006.47-702820.4	361.5	3906	5719.3±0.8	286.5±0.3	75.4±14.4	274.7±2.9	0.172±0.006	4.270±0.046	0.630±0.077	4.544±0.099	1.31±0.07	0.82±0.07	74.3	115.2	0.8	1032.0	0.5
<b>eccentric orbits (Nicholls &amp; Wood (2012))</b>																	
052013.51-692253.2	452.5	4027	388.4±1.5	248.0±1.5	60.2±1.4	339.8±12.6	0.412±0.006	2.846±0.032	0.719±0.095	6.076±0.333	1.50±0.19	1.08±0.15	73.2	138.6	1.1	1189.1	2.0
052438.40-700028.8	411.0	4125	321.5±0.6	271.4±0.3	90.0	527.3±3.7	0.117±0.005	4.284±0.039	0.675±0.012	4.658±0.037	6.96±0.16	4.70±0.11	137.9	218.0	2.8	4787.1	518.2
052812.41-693417.9	258.7	3936	638.2±0.7	254.1±1.1	90.0	234.6±8.1	0.236±0.007	3.855±0.043	0.578±0.064	4.807±0.219	1.64±0.18	0.95±0.12	59.4	100.2	0.9	688.7	0.9
052850.12-701211.2	662.2	3796	-52.8±0.9	244.4±0.1	51.9±0.9	581.4±2.8	0.256±0.005	3.436±0.021	0.894±0.023	4.988±0.045	3.18±0.06	2.84±0.06	160.9	225.9	2.7	4073.4	77.5
053033.55-701742.0	390.2	4081	800.6±0.3	250.4±0.1	54.4±2.2	480.6±2.5	0.207±0.004	5.090±0.019	0.593±0.028	4.612±0.038	6.15±0.15	3.65±0.12	127.5	204.2	2.3	3872.6	200.8
053124.49-701927.4	541.3	3848	420.8±1.8	244.0±0.2	90.0	416.0±4.6	0.368±0.009	3.338±0.038	0.464±0.011	5.350±0.058	2.25±0.08	1.05±0.04	92.9	185.8	1.0	1473.2	1.4
053159.96-693439.5	501.1	3969	888.3±1.1	242.3±0.2	90.0	480.7±3.8	0.388±0.006	4.509±0.025	0.369±0.008	4.918±0.041	4.34±0.10	1.60±0.05	116.4	224.5	1.3	2774.7	8.8

After finding the best solution according to the procedure above, we further refined the solution by correcting the input parameters of the secondary star. The initial values of these parameters were roughly estimated using Equations 1 to 10, which include the assumption that the secondary star was in the middle of main sequence evolution for a star of its mass. After the derivation of the orbital solution with the initial parameter values, the evolutionary status of the secondary was improved by utilizing the fact that both of the components were born at the same time and have the same age. Using the evolutionary tracks of Bertelli et al. (2008) and the values of  $m_1$ ,  $L_1$  and  $T_{\text{eff1}}$  obtained from the WD code, we estimated the age of the red giant and this age was used to determine  $L_2$  and  $T_{\text{eff2}}$  since we know  $m_2$  from the first orbital solution. We then estimated the contribution of each stellar component to the total  $I$  flux of the system. In all cases, the secondary contribution to the total  $I$  flux was less than 4% and mostly less than 1%, meaning that the amplitude of the ellipsoidal light variations in  $I$  is not altered by an amount detectable with the current observations of the  $I$  light curve. However, in a small number of stars, the depths of eclipses could be affected at a detectable level ( $\geq 0.003$  mag.). In these cases, the orbital solutions were re-computed using the values of  $T_{\text{eff2}}$  and  $\Omega_2$  obtained from the parameters of the first solution. We also checked whether the light from the secondary could affect our derivation of  $T_{\text{eff1}}$  from  $I-K$ , which was made under the assumption that all the  $I$  and  $K$  flux from the system came from the red giant primary. In one system (OGLE 052913.51-695632.3), the secondary causes a change of  $\sim 50$  K in  $T_{\text{eff1}}$  while the change for all other objects is  $\lesssim 20$  K and mostly  $\lesssim 10$  K. Since these changes are less than the estimated error in  $T_{\text{eff1}}$  of 100 K (see subsection 3.5), we did not make any changes to  $T_{\text{eff1}}$ .

We attempted to model 97 objects in total but for various reasons 16 objects were rejected. Detailed remarks noting the reasons for rejection are given in subsection 3.4. The parameters of the solutions for the successfully modelled objects (81

in total) are given in Table 1 along with standard errors for the parameters. We only provide values of  $L_2$  and  $R_2$  to 0.1 solar units since changes of this size do not affect the solution at a detectable level and the only parameter for the secondary star that we derive from the orbital solutions is  $m_2$ . The light and velocity curve fits for all the successful solutions are shown in Figure 1. The full version of Figure 1 is provided online.

### 3.3. A check on error estimation by the WD code

The referee of this paper expressed doubts about the reliability of the error estimates given by the WD code. In order to provide independent error estimates for the model parameters, we have used an adaptive Markov chain Monte Carlo (MCMC) method to examine the distribution of likely parameter values.

The basic MCMC code we used is that described by Haario et al. (2001) and Haario et al. (2006)<sup>4</sup>. The user provides the residual sum of squares function for which we used the value given by the WD code. The residual sum of squares was normalized to the value for the best WD model so that the normalized value gives  $-\ln(p)$ , where  $p$  is the likelihood of the model relative to the best model. For each set of model parameters proposed by the MCMC code, the WD code was run to obtain the residual sum of squares and the process was repeated for the defined number of proposals. Since tens of thousands of proposals are required to generate a useful probability density function when six (circular orbits) or eight (eccentric orbits) parameters vary, the method is quite computationally expensive.

In Figures 2 and 3, we illustrate the results of our MCMC simulations for OGLE 050222.40-691733.6, which has a circular orbit, and OGLE 050610.03-683153.0, which has an eccentric orbit. We generated 50000 proposals for the first object and 30000 for the second. In both figures, there are clear correlations between some parameter, for example  $q$  and  $i$ , as well as some forbidden regions ( $i > 90$ , or combinations of  $\Omega_1$  and  $a$  that overfill the Roche Lobe). In all cases, the most

<sup>4</sup> The fortran 90 code is available at <http://helios.fmi.fi/~lainema/mcmcf90/>.

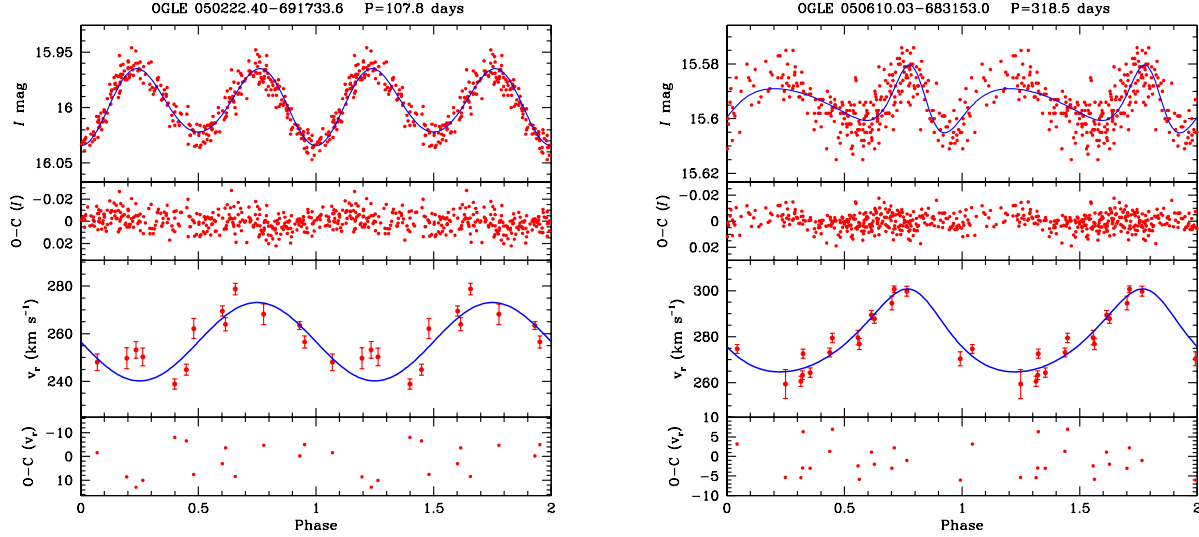


FIG. 1.— Fits of the light and velocity curves with the best solution. In the top and third panels, red points are the observations and blue curves are the fits for light and velocity curves, respectively. In the second and bottom panels, red points are the fitting residual for light and velocity curves. The two examples are the first object of Table 1 with circular and eccentric orbits, respectively. The fittings of the whole sample are provided online.

likely parameter values estimated from the marginal distributions on the diagonals of the figures agree with the values from the WD code to less than one standard deviation as estimated by the WD code. In fact the agreement is to within a small fraction of one standard deviation except possibly for  $q$  where the marginal distribution has a large skewness. Note also that the standard deviations estimated by the WD code and the MCMC analysis agree well, once again with the possible exception of  $q$  due to the highly skewed distribution resulting from the MCMC analysis.

We have run the MCMC code for a small number of other objects and find similar results to those shown for OGLE 050222.40 -691733.6 and OGLE 050610.03 -683153.0 (to run the MCMC code on all 81 objects would be too computationally expensive). Our conclusion is that both the parameter estimates and the standard errors given by the WD code are reliable.

### 3.4. Rejected objects

We rejected the orbital solutions of 16 objects. The reasons for rejection are given below for each of these objects:

*OGLE 050107.08 -692036.9* — The solution only converged for  $i =$  near 90 degrees, with derived mass  $m_1 \sim 1.9 M_\odot$  and  $q > 1$ , and for these solutions the fitting of the light and radial velocity curves is not good. Since  $T_{\text{eff}1} = 5773$  K, the primary star is a hot star. A star of this temperature should be in the pre-RGB phase. It is unlikely to be in the He core burning phase, as it would have been larger earlier in its life. It could also be a post-AGB star in principle, but this is unlikely because  $m_1$  is much larger than the post-AGB star mass ( $\sim 0.55 M_\odot$ ) for the observed luminosity of  $3278 L_\odot$ . If it is on the pre-RGB, it needs  $m_1 \sim 6.5 M_\odot$  to match the observed luminosity. However, the solution has  $m_1 < 2.0 M_\odot$ .

*OGLE 050334.97 -685920.5* — From the relatively hot effective temperature (5666 K) and the observed luminosity ( $2526 L_\odot$ ), this star should be on the pre-RGB phase with

mass  $\sim 6.3 M_\odot$ . However, the large velocity amplitude and relatively short period require  $m_1 \sim 2.6 M_\odot$  and a large mass for  $m_2$  ( $\sim 7 M_\odot$ ), so that  $q > 1$ . We are unable to get an acceptable solution for this object.

*OGLE 050454.49 -690401.2* — This is a hot star and the effective temperature (6017 K) and luminosity ( $5175 L_\odot$ ) are consistent with a pre-RGB star of mass  $7.0 M_\odot$ . However, the large velocity amplitude and long period require a large mass for  $m_2$  ( $\geq 10 M_\odot$ ) so that  $q > 1$ . We are unable to get an acceptable solution for this object.

*OGLE 050758.17 -685856.3* — The solution with  $i \sim 75$  degrees has the lowest light curve dispersion, but the calculated  $m_1$  ( $7.88 M_\odot$ ) is too large since even at the base of the giant branch the evolutionary track for this  $m_1$  gives a luminosity that is larger than the observed luminosity. For the observed luminosity of this object, evolutionary tracks require the mass of  $m_1$  to be less than  $7.0 M_\odot$ .

*OGLE 050800.52 -685800.8* — This is similar to the previous object. The mass of  $m_1$  should be less than  $8.0 M_\odot$ , but the derived solution shows  $i \sim 71$  and  $m_1 = 9.12 M_\odot$ .

*OGLE 051515.95 -685958.1* — We were not able to get a solution to fit the two very different light maxima.

*OGLE 051845.02 -691610.5* — All solutions have  $q \gg 1$  and  $R_1 \ll R_{L,1}$  (meaning no stable mass transfer is possible), with the best solution having  $i \sim 60$  degrees,  $m_1 \sim 0.8 M_\odot$  and  $m_2 \sim 1.9 M_\odot$ .

*OGLE 052032.29 -694224.2* — This is a hot star with  $T_{\text{eff}1} = 5972$  K, suggesting the star is in the pre-RGB phase. Given the luminosity of  $2569 L_\odot$ ,  $m_1$  should then be  $\sim 6 M_\odot$ . The orbital solutions have about half this mass for  $m_1$ . We are unable to find an acceptable solution for this object.

*OGLE 052048.62 -704423.5* — From the light curve and low amplitude velocity curve, this appears to be a pulsator of very low amplitude, not an ellipsoidal binary.

*OGLE 052203.16 -704507.8* — The orbital solution requires  $m_1 < 0.4 M_\odot$ , which is too low a mass for the star to have

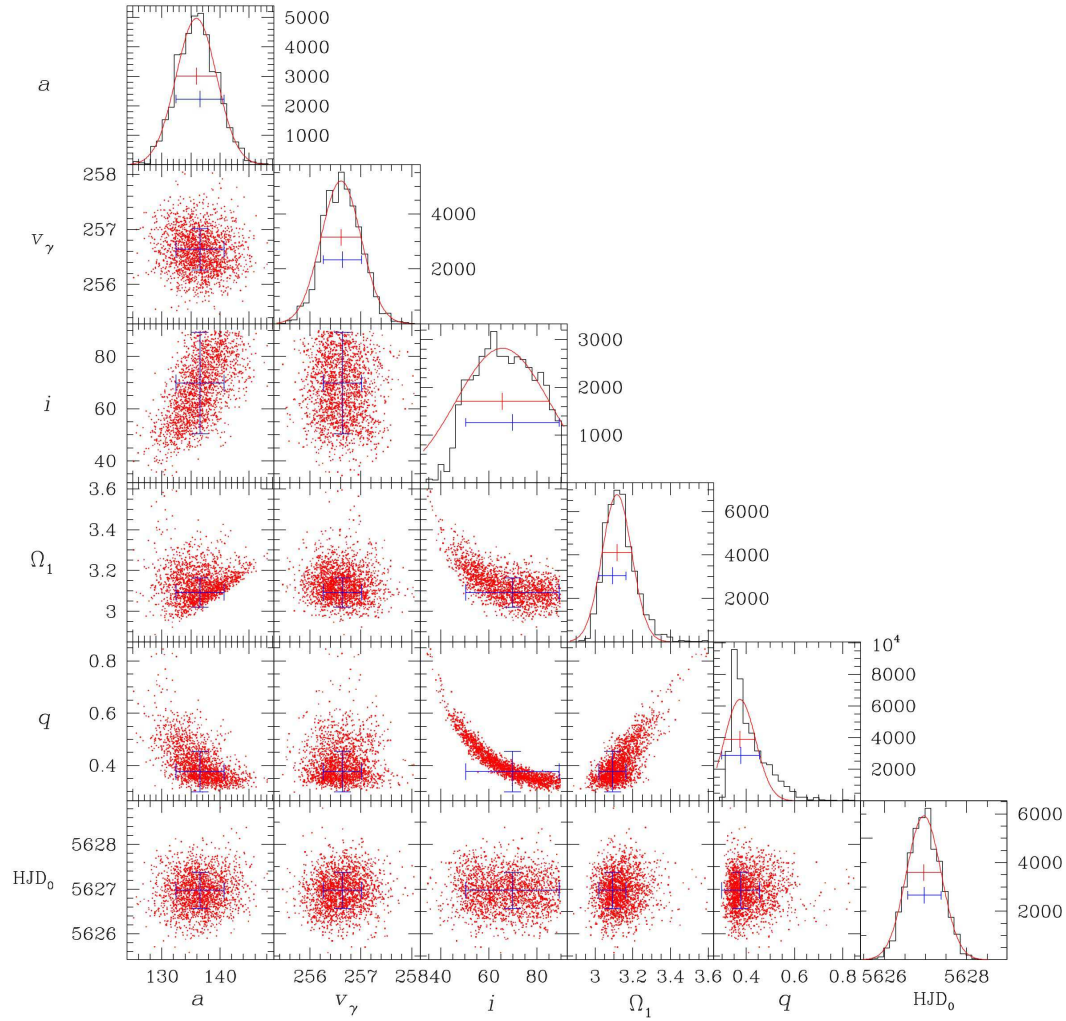


FIG. 2.— The results of MCMC simulation for OGLE 050222.40 -691733.6. The scatter plot panels below the diagonal show one red point for each proposed pair of values of the two parameters pertaining to the panel. The density of points is proportional to the probability that the parameters could produce the observed radial velocity and  $I$  values. Clear correlations between some pairs of parameters are seen. The panels on the diagonal of the plot show the marginal distribution (black histogram) of the associated parameter for all proposals in the MCMC simulation. A gaussian has been fitted to points in the marginal distribution with values more than 25% of the maximum (red curve) and the mean value and  $1\text{-}\sigma$  error bars are shown (red line). The blue error bars are the  $1\text{-}\sigma$  error estimates given by the WD code.



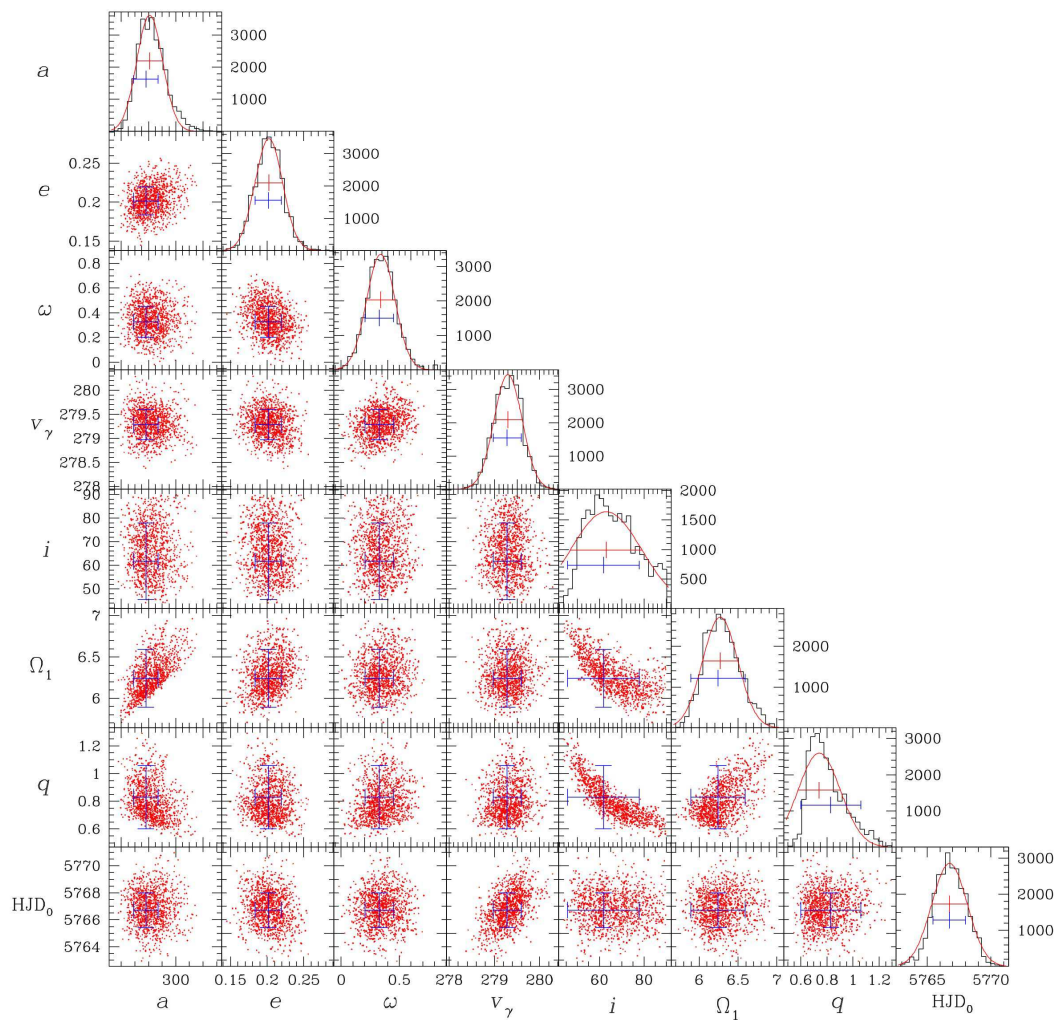


FIG. 3.— The same as Figure 2 but for the OGLE 050610.03 - 683153.0, which has an eccentric orbit.



evolved off the main sequence. In addition, the observed velocity curve shows inconsistent points (sharp dip, low amplitude) and the scatter of the light curve suggests pulsation. This is possibly a sequence D star (Wood et al. 1999; Nicholls et al. 2010).

*OGLE 052228.84-694313.8* — We were not able to get an acceptable solution to fit the two light maxima of different brightness. This is the same problem that we encountered for *OGLE 051515.95-685958.1*.

*OGLE 052458.88-695107.0* — The light curve suggests pulsation and the velocity amplitude is about  $5 \text{ km s}^{-1}$ , only a little larger than the mean error of all the data ( $2 \text{ km s}^{-1}$ ). Once again, this is probably a sequence D star.

*OGLE 052513.34-693025.2* — This is a very small amplitude object so the photometry errors are large compared to the amplitude. It is impossible to put any meaningful constraint on the inclination.

*OGLE 052757.39-693901.7* — This is an object from Nicholls et al. (2010). The light curve amplitude is large, up to 0.6 mag in the *I* band, very different from all the other ellipsoidal red giant binaries in this paper. The system seems to be an eclipsing pair of red giants. The strategy described in section 3 for orbit solutions is not applicable to this binary system. Owing to this, we set the gravity darkening exponent  $g_2 = 0.35$  and the bolometric albedo  $A_2=0.5$  (appropriate for a red giant secondary) and adjusted  $T_{\text{eff}1}$ ,  $T_{\text{eff}2}$ ,  $\Omega_1$  and  $\Omega_2$  to get a solution. The solution only converged at  $i = 90$  and  $80$  (with strong eclipses), with very good fitting. The secondary red giant has a mass similar to that of the primary red giant, but it has a smaller size and fainter luminosity. Due to the somewhat arbitrary selection of input parameters and the unusual nature of this object, we reject the solution.

*OGLE 052928.90-701244.2* — The light curve of this star shows a large pulsation amplitude along with the binary ellipsoidal light variations. In addition, the data quality of the whole light curve is poor, so it is hard to determine the orbital period. Its periods from *OGLE II* data and *MACHO* data are different. When using the period determined from *OGLE II* data,  $i = 50$  gives the best solution. However, then the mass  $m_1 \sim 0.35 M_{\odot}$ , too low for a red giant.

*OGLE 053219.66-695805.0* — From the *OGLE II* finding chart, there are two stars  $1.3''$  apart, too close for the *WiFeS* (Wide Field Spectrograph) instrument (Dopita et al. 2007, 2010) to resolve consistently, so the radial velocity curve might be a combination of these two stars.

### 3.5. The effect of $T_{\text{eff}}$ , gravity brightening, limb darkening and distance modulus on orbital parameters

In the modelling process, the red giant size is determined by the assigned values of  $T_{\text{eff}1}$  and  $L_1$ . For an observed amplitude of ellipsoidal light variability, the assigned size of the red giant will clearly affect the derived orbital separation and this will in turn affect the derived masses for the given orbital period. Here, we examine the effect of  $T_{\text{eff}1}$  and adopted distance modulus (DM), which affects  $L_1$ , on derived orbital parameters. Also, since the relative depths of the alternating minima depend on the amount of gravity brightening and the limb darkening (see subsection 3.2), we examined the effect of the gravity brightening exponent  $g_1$  and the limb darkening law (LD) on the orbital solutions. We illustrate the effects using the system *OGLE 050222.40-691733.6* and the results are shown in Table 2. For each set of input values of  $T_{\text{eff}1}$ ,  $g_1$ , LD and DM, the derived orbital parameters are given along

with the standard error  $\sigma$  given by the WD code.

Model 1 is the reference model obtained using standard parameters. Model 2 shows the effect of increasing the assigned value of  $T_{\text{eff}1}$  by 100 K. We note that  $T_{\text{eff}1}$  is derived from the *I-K* color and the relation between *I-K* and  $T_{\text{eff}}$  given in Houdashelt et al. (2000a) and Houdashelt et al. (2000b). A change of 100 K for  $T_{\text{eff}}$  values around  $T_{\text{eff}} \sim 4000 \text{ K}$  corresponds to a change in *I-K* of  $\sim 0.1$ . The observed average value of *I* obtained from the *OGLE* light curve is very accurate with an error less than 0.01 mag. The *K* value from 2MASS was taken at a random orbital phase so that the measured value could differ from the mean value by up to half the *K* amplitude. Since the median *K* amplitude of our objects is 0.048 mag (we assume the *K* amplitude is equal to the *I* amplitude, which is readily obtained from the *I* light curve), the maximum difference between the observed and average values of *K* should be typically  $0.5 * 0.048 = 0.024 \text{ mag}$ . The photometric errors in *K* range from  $\sim 0.02 - 0.09 \text{ mag}$  for the brightest to the faintest objects. Thus the maximum expected total error in *K* and *I-K* is  $\sim 0.1 \text{ mag}$ , the latter corresponding to a maximum error in  $T_{\text{eff}1}$  of  $\sim 100 \text{ K}$ .

It can be seen from Table 2 that increasing  $T_{\text{eff}1}$  by 100 K decreases the size of the red giant and the orbital separation by  $\sim 5\%$ , the mass  $m_1$  by  $\sim 16\%$  ( $\sim 1.6 \sigma$ ) and the mass  $m_2$  by  $\sim 10\%$  ( $\sim 0.4 \sigma$ ).

As shown in Alencar & Vaz (1997), the gravity brightening exponent  $g_1$  varies with  $T_{\text{eff}}$ . In model 3, we examine the effect of changing  $g_1$  by 0.026, which corresponds to the change in  $g_1$  for an increase in  $T_{\text{eff}}$  of 100 K, and which is also similar to the scatter in the derived values of  $g_1$  at a given temperature around 4000 K in the models of Alencar & Vaz (1997). The results in Table 2 show that changes in  $g_1$  of this size have almost no effect on the derived orbital parameters. Since  $T_{\text{eff}}$  and  $g_1$  are correlated, in model 4 we show the effect of the combined change in  $T_{\text{eff}}$  and  $g_1$ . It can be seen that the solution parameters are close to those resulting from the change in  $T_{\text{eff}}$  alone.

Models 1, 5 and 6 show the effects that changes in the limb darkening law make to the derived orbital parameters. Model 1 uses our standard assumption of a square root law (LD = -3 in the WD code), model 5 uses a logarithmic law (LD = -2) and model 6 used a linear cosine law (LD = -1). It can be seen that the adopted limb darkening law makes almost no difference to the solution parameters.

Finally, we examined the uncertainties caused by the uncertainty in the LMC distance modulus. Note that in this paper we use a distance modulus of 18.49 (de Grijs et al. 2014) whereas in our data paper (Nie & Wood 2014) we used a distance modulus of 18.54 (Keller & Wood 2006). Model 7 in Table 2 shows the effect of increasing the distance modulus by 0.05. This change leads directly to a slightly larger luminosity and radius for the red giant and subsequently to slightly larger values for  $a$ ,  $m_1$  and  $m_2$ . The masses  $m_1$  and  $m_2$  increase by  $\sim 4\%$ , well with the  $1-\sigma$  standard errors for these quantities.

In summary, it seems that the uncertainties in  $T_{\text{eff}}$  have the greatest influence on the orbital solution parameters. The estimated maximum uncertainty in  $T_{\text{eff}1}$  of 100 K could lead to uncertainties in  $m_1$  and  $m_2$  of  $\sim 16\%$  and  $\sim 10\%$ , respectively, corresponding to  $\sim 1.6 \sigma$  and  $0.4 \sigma$ . Note that the errors given in Table 1 are model fit errors only and they do not include the additional uncertainties arising from uncertainties in  $T_{\text{eff}}$ , gravity darkening, limb darkening and distance modulus, which have been discussed here.

TABLE 2  
THE EFFECT OF  $T_{\text{eff}}$ ,  $g_1$ , LIMB DARKENING AND DISTANCE MODULUS ON ORBITAL PARAMETERS OF OGLE 050222.40 -691733.6

Model	DM	$T_{\text{eff}}$ K	$R_1$ $R_{\odot}$	$g_1$	LD	$a$ $R_{\odot}$	$q$	$i$ deg	$m_1$ $M_{\odot}$	$m_2$ $M_{\odot}$
1	18.49	3990	51.59	0.301	-3	136.6±4.1	0.3765±0.0781	69.8±19.5	2.139±0.230	0.805±0.188
2	18.49	4090	48.28	0.301	-3	129.8±3.8	0.4027±0.0826	70.2±19.3	1.803±0.192	0.726±0.168
3	18.49	3990	51.53	0.327	-3	136.8±4.6	0.3847±0.1048	67.3±22.9	2.136±0.271	0.822±0.247
4	18.49	4090	48.28	0.327	-3	130.4±4.0	0.3998±0.0841	70.3±19.9	1.832±0.200	0.732±0.174
5	18.49	3990	51.60	0.301	-2	136.7±4.1	0.3762±0.0779	69.8±19.4	2.143±0.229	0.806±0.188
6	18.49	3990	51.59	0.301	-1	136.3±4.1	0.3778±0.0777	69.8±19.2	2.124±0.227	0.802±0.186
7	18.54	3990	52.72	0.301	-3	138.4±4.6	0.3795±0.1011	67.1±22.2	2.220±0.276	0.842±0.248

#### 4. ANALYSIS OF RESULTS

Table 1 provides orbital solutions for a large number (81) of ellipsoidal red giant binaries in the LMC, which we refer to hereinafter as our sample. We now analyse the properties of our sample.

##### 4.1. The evolutionary status of the red giant primaries

In general, our sample consists of binaries of two types: (1) those containing low mass red giants ( $m_1 \leq 1.85 M_{\odot}$ ) which are evolving on the RGB or AGB with degenerate He or C/O cores, respectively, and (2) those containing intermediate mass red giants ( $1.85 M_{\odot} \leq m_1 \leq 8.0 M_{\odot}$ ) evolving with non-degenerate He cores prior to core He burning or evolving on the AGB after core He burning (since red giants shrink after He ignition in the core, it is unlikely that they would be ellipsoidal variables during the core He burning phase).

Figure 4 shows our red giant binaries in the HR diagram with the masses indicated by symbols of different size and color. Evolutionary tracks for stars of selected masses are also shown. Here, a metallicity of  $Z = 0.008$  is used for the tracks of the younger stars with  $M \geq 3 M_{\odot}$  while a metallicity of  $Z = 0.004$  is used for the older stars of  $M=0.8, 1.5$  and  $1.85 M_{\odot}$  in order to take account of the age-metallicity relation for LMC stars (Piatti & Geisler 2013). In general, the masses derived for the red giants fall in the positions expected from evolutionary tracks, although there will be some scatter caused by errors in the determined mass and by metallicity variations. We note that these results, together with recent asteroseismological results from Kepler and CoRoT (e.g. Kallinger et al. 2010; Stello et al. 2013), provide rare tests for the positions of red giants with a wide range of masses in the HR diagram.

In Figure 5, we show our sample of ellipsoidal variables in the Period-Luminosity diagram, with the masses  $m_1$  for each system indicated by the symbol color and size. The red giant mass generally increases as the luminosity increases at a given period. This verifies the suggestions of Soszynski et al. (2004) and Nie & Wood (2014) that, because higher mass systems will have larger separations at a given orbital period, the red giant primaries in them will need to get to a higher luminosity (radius) to produce detectable ellipsoidal light variations. Note that our sample is somewhat biased to higher masses as Nie & Wood (2014) deliberately chose extra objects on the high-luminosity side of the PL sequence in order to get a reasonable number of intermediate mass stars in the sample.

Metallicity should also affect the position of a binary system on the PL sequence. If we consider two systems with stars of the same mass but different metallicity, then the orbital periods and separations will be the same but the one with lower metallicity will have a smaller red giant at a given luminosity,

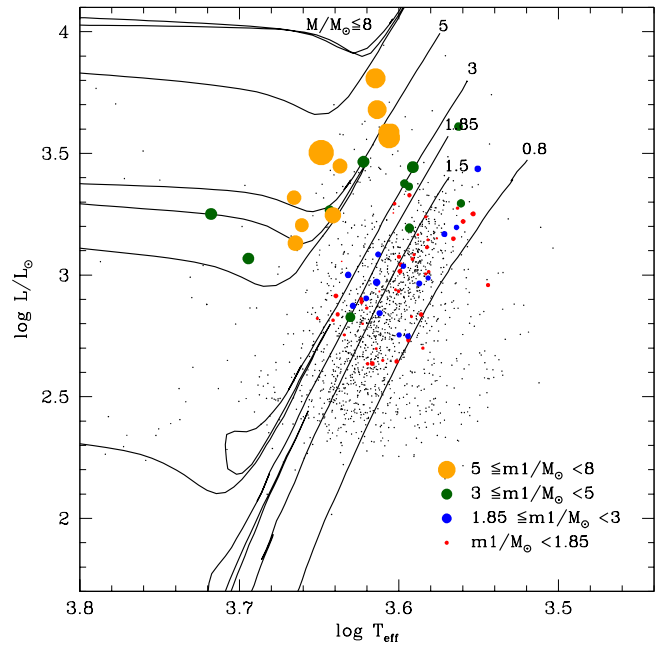


FIG. 4.— The HR diagram for red giant ellipsoidal variables. Ellipsoidal variables belonging to the full sample in Soszynski et al. (2004) are shown as black dots, with  $T_{\text{eff}}$  and  $\log L/L_{\odot}$  obtained from  $I$  and  $K$  photometry as described in Nie et al. (2012). The objects in our sample are shown by symbols whose color and size depends on the red giant mass. The symbol diameter is proportional to mass  $m_1$ . The evolutionary tracks of Bertelli et al. (2008) are shown as black lines. For the 0.8 and 1.5  $M_{\odot}$  tracks, the evolution is shown only to the RGB tip while for the more massive tracks AGB evolution to near the first thermal pulse is included as well.

so the red giant will need to get to a higher luminosity to reach the radius required to produce detectable ellipsoidal light variations. This will lead to relatively lower masses on the higher luminosity side of the PL sequence for lower metallicity stars. Examples of such stars can be seen in Figure 5, especially for the systems with  $m_1 < 1.85 M_{\odot}$ .

Finally, we note that in addition to systematic variations in mass at a given period in the PL diagram, a mass dispersion is also expected. This is because ellipsoidal variations can be detected over a range of values for the Roche lobe filling factor. Hence, for an individual system with a given orbital period, ellipsoidal variations will be detectable over a range in luminosities. The ellipsoidal light amplitude should increase with luminosity in this system. This effect was confirmed by Soszynski et al. (2004) who demonstrated that higher amplitudes of ellipsoidal light variations were shown by stars on the higher luminosity side of the PL sequence. The origin of the higher light amplitude is a larger Roche lobe filling factor  $f$ .

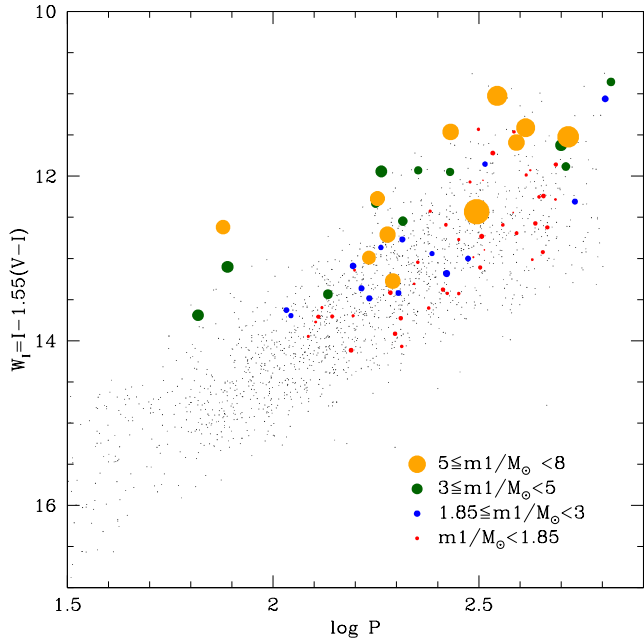


FIG. 5.— The Period-Luminosity diagram for ellipsoidal variables showing how position depends on the red giant mass  $m_1$ .  $W_I$  is a reddening-free Weisenheit index (Madore 1982) that is essentially a measure of luminosity and  $P$  is the orbital period in days. Symbols are the same as in Figure 4.

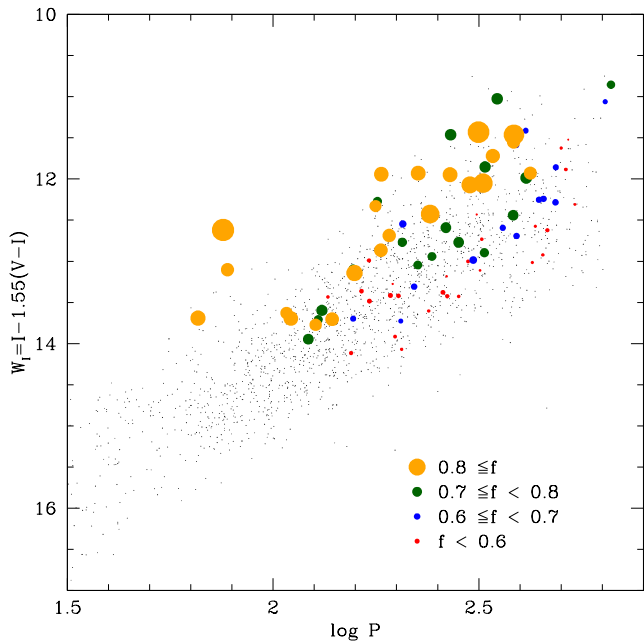


FIG. 6.— The Period-Luminosity diagram similar to Figure 5 except that the symbol sizes and colors now indicate the Roche lobe filling factor  $f$ , with symbol diameter proportional to  $f^3$ .

Since we determine  $f$  for all the stars in our sample we can test this assumption directly. Figure 6 shows the PL diagram with the value of  $f$  for our sample indicated by the symbol size and color. There is a clear increase in  $f$  to the high luminosity side of the PL sequence, as expected. By comparing Figure 5 and Figure 6 it can be seen that the systems with the larger values of  $f$  are not necessarily the ones with higher

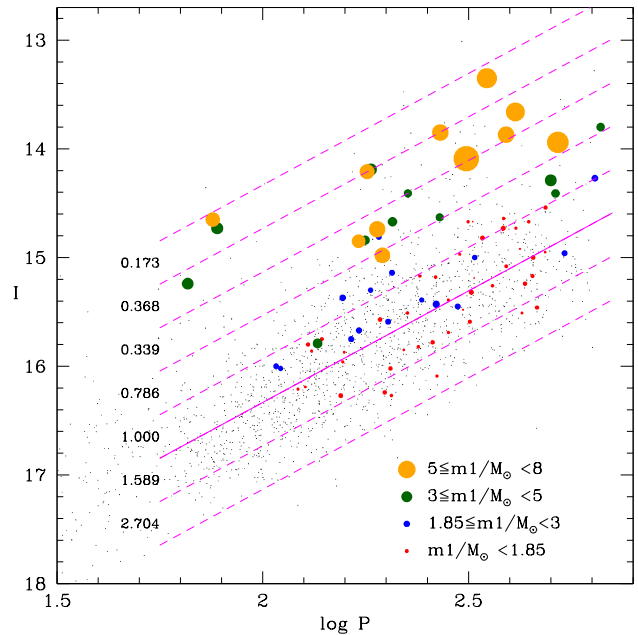


FIG. 7.— The  $I$ - $\log P$  diagram with symbols as in Figure 4. The solid pink line is a fit in the interval  $1.75 < \log(P) < 2.85$  to the sample of ellipsoidal variables in Soszynski et al. (2004) (black dots). The dashed lines are spaced from the solid line at intervals of 0.4 magnitudes in  $I$  and the numbers in the left part of the plot are the weights applying to observed systems lying between the adjacent pair of lines.

mass.

#### 4.2. The primary mass distribution

As noted in Nie & Wood (2014), our sample of observed objects was selected from the  $I$ - $\log P$  plane. The objects for which we were able to derive complete solutions are shown in this plane in Figure 7 where the red giant mass  $m_1$  is indicated by the symbol color and size. It is clear that  $m_1$  depends strongly on position in this diagram (as it did in the  $W$ - $\log P$  plane, Figure 5).

The top panel of Figure 8 shows the raw distribution of red giant masses for all objects in our full sample. This distribution is biased by observational selection, especially by the deliberate selection of brighter objects at a given period by Nie & Wood (2014) and by the relatively bright objects from Nicholls & Wood (2012). Our aim is to make an unbiased estimation of the distribution of primary red giant masses in the full sample of LMC ellipsoidal variables of Soszynski et al. (2004). The full sample of the ellipsoidal variables (the sequence E stars) are shown in Figure 7 as small black dots. The solid pink line is a linear fit to this sample in the interval  $1.75 < \log(P) < 2.85$ .

Looking at Figure 7, we see that the masses  $m_1$  of stars in our sample appear to be roughly similar on lines parallel to the  $I$ - $\log P$  sequence formed by the black dots in Figure 7 i.e. on lines parallel to the solid pink line. At a given period, the more massive stars are brighter so that without a correction for the preferential selection of brighter object, the raw mass distribution will over-emphasize the number of high mass objects.

In order to attempt to remove our selection bias towards brighter objects at a given period, we have divided the  $I$ - $\log P$  plane into strips parallel to the  $I$ - $\log P$  sequence, with the strip

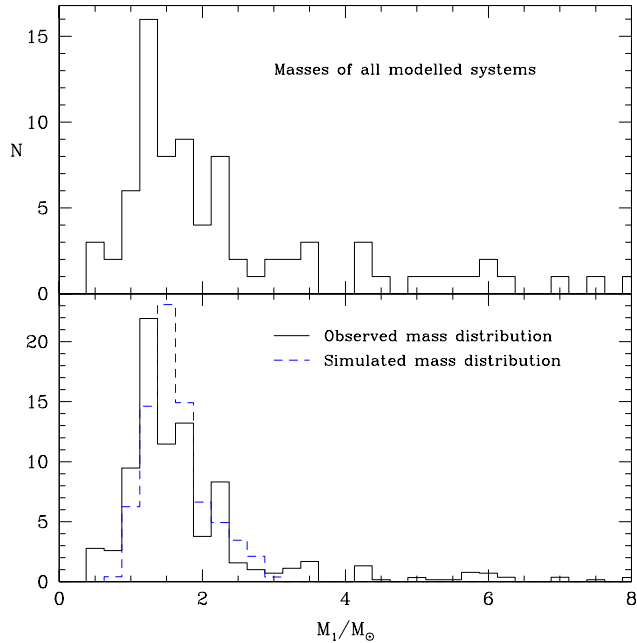


FIG. 8.— Distribution of the primary mass. The top panel shows the raw distribution for all red giant masses in our sample while the bottom panel shows the distribution adjusted for selection bias as described in the text. Also shown in the bottom panel is the equivalent distribution of red giant masses in sequence E stars according to a simulation based on the method of Nie et al. (2012). The simulated distribution is normalized to have the same number of objects with  $m_1 < 3 M_\odot$  as the observed distribution.

width being 0.4 magnitudes in  $I$ . In each of these strips there are a number of objects from our sample for which we have estimates of  $m_1$ , as well as many objects from the sample of Soszynski et al. (2004). In order to estimate the mass distribution in the unbiased sample of Soszynski et al. (2004) in the interval  $1.75 < \log(P) < 2.85$ , where our objects lie, we assign to each of our objects in a given strip a weight  $w_i$  which is the ratio of the number of Soszynski et al. (2004) objects with  $1.75 < \log(P) < 2.85$  in the strip to the number objects from our sample in this strip, scaled by a common factor. These weights are shown in Figure 7 on the left side of each strip, and they clearly show our preferential selection of brighter objects. Applying these weights, we derive a histogram showing our estimate of the distribution of red giant masses in the sample of Soszynski et al. (2004) in the interval  $1.75 < \log(P) < 2.85$ . This histogram is shown in the bottom panel of Figure 8 where the number of objects assigned to each bar of the histogram is  $\sum_i w_i$  for all those objects  $i$  whose  $m_1$  lies between the mass limits for the bar of the histogram.

Also shown in the bottom panel of Figure 8 is the distribution of red giant masses expected for sequence E stars according to a simulation based on the modelling prescriptions described in Nie et al. (2012). We have assumed that the comparison sample of sequence E stars from the simulation consists of all observable sequence E stars brighter than  $M_{\text{bol}} = -1.6$  (i.e. two magnitudes below the tip of the RGB at  $M_{\text{bol}} = -3.6$ ) but excluding low mass stars ( $m_1 < 1.85 M_\odot$ ) that are on the AGB and which have become more luminous than the RGB tip. These stars were excluded because they are observed to be pulsationally variable (e.g. Wood 2015) and their ellipsoidal variability will be difficult to detect when

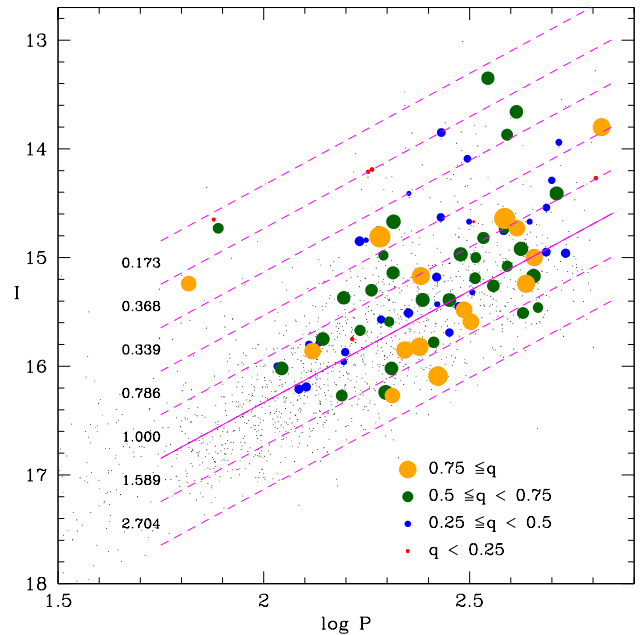


FIG. 9.— The same as Figure 7 except that the colored symbols indicate the  $q$  value.

combined with semiregular pulsational variability.

Comparing the raw mass distribution of the red giants (top panel of Figure 8) with the estimated true distribution (bottom panel), it can be seen that the raw observed sample is biased towards the brighter, more massive stars. This bias was described by Nie & Wood (2014) for their sample and is further enhanced by the inclusion of the sample of objects from Nicholls & Wood (2012). The procedures noted above should have corrected our estimated true mass distribution for this bias.

In the bottom panel of Figure 8 there is good agreement between the estimated true current red giant mass distribution and the equivalent simulated mass distribution. Note that the simulation only considers stars with initial masses up to  $3 M_\odot$  so we can only compare the observed and simulated mass distributions up to this mass. A characteristic property of both distributions is that each shows a peak at a current red giant mass of  $\sim 1.5 M_\odot$ . This provides direct confirmation that the mass distribution of the primary masses in binary systems with periods of  $\sim 100$ – $1000$  days is similar to that of the single stars in the LMC. The single star mass distribution in the LMC is dominated but a burst of star formation in the interval  $0.5$ – $4$  Gyr ago and this star formation history was used in the models of Nie et al. (2012) as well as here.

#### 4.3. The mass ratio distribution

In Figure 9 we show the mass ratio  $q = m_2/m_1$  for our sample plotted on the  $I$ - $\log P$  plane in order to see if there is any preferential position for large or small  $q$  values that could lead to a selection bias, as was found in the case of  $m_1$ . The different  $q$  values appear to be spread uniformly across the  $I$ - $\log P$  sequence formed by the complete OGLE II sample of Soszynski et al. (2004), unlike the masses  $m_1$ . In Figure 10,  $q$  is plotted against  $m_1$  to show the dependence of  $q$  on  $m_1$ . A two-sample KS test on the data divided into two at  $m_1 < 3 M_\odot$  and  $m_1 \geq 3 M_\odot$  gives a probability of 10% that the more and less massive samples come from the same



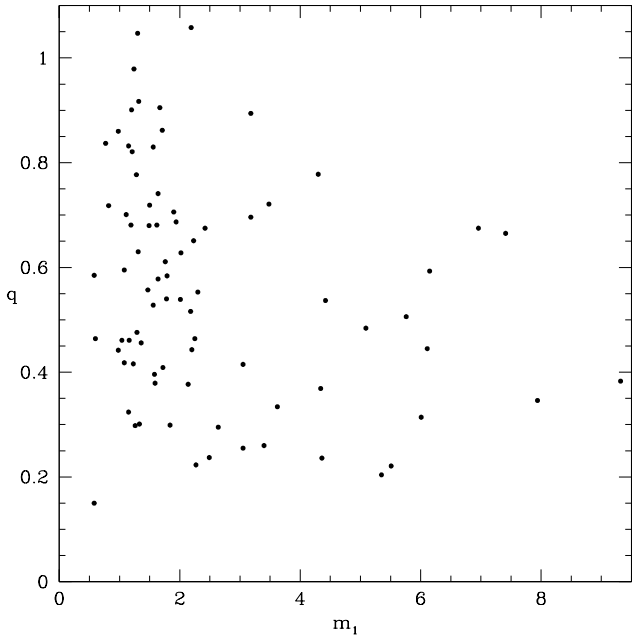


FIG. 10.— The  $q$  value plotted against  $m_1$  for the sequence E stars in our sample.

underlying distribution, which implies that there is a reasonable probability that binaries with  $m_1 \geq 3 M_\odot$  have lower  $q$  values than binaries with less massive primaries. Similarly, comparing the systems where the primary star was originally an F or G star ( $m_1 < 1.4 M_\odot$ ) with the systems where the primary was originally an A or late-B star ( $3 > m_1 > 1.4 M_\odot$ ) gives a probability of 47% that the two samples come from the same underlying distribution. Thus we have no evidence that  $q$  depends on  $m_1$  in the mass range  $m_1 < 3 M_\odot$ .

The raw distribution of  $q$  values for our complete sample is shown in Figure 11. In an attempt to remove any bias due to the selection of bright objects, we applied the same weighting scheme to the objects that was used for the  $m_1$  values in order to get a distribution that is selected uniformly from the sample of Soszynski et al. (2004) in the  $I$ - $\log P$  plane in the interval  $1.75 < \log(P) = 2.85$ . This distribution is also shown in Figure 11.

We aim to compare the  $q$  distribution for our sample of red giant binaries with other observed distributions. The two most comprehensive observed binary mass ratio distributions are those of Duquennoy & Mayor (1991) and Raghavan et al. (2010) which apply to stars in the solar vicinity. In both these studies, the primary stars are on the main sequence whereas in our case the primary star is a red giant that has undergone some mass loss so that the current mass ratio is different from that on the main sequence. Also, the detection of ellipsoidal variability, and hence the lifetime of a sequence E star, depends on the mass ratio. These factors need to be taken into account when comparing our sample to those of Duquennoy & Mayor (1991) and Raghavan et al. (2010). We do a comparison with the Duquennoy & Mayor (1991) distribution by running a simulation based on the prescriptions of Nie et al. (2012) as described in subsection 4.2. This simulation estimates the distribution of  $q$  values of sequence E stars in the full sample of Soszynski et al. (2004) when starting on the main sequence with the  $q$  distribution of

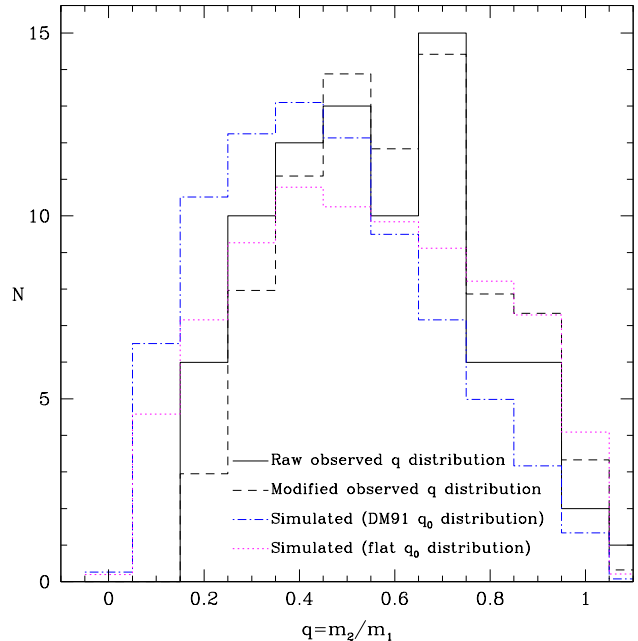


FIG. 11.— Distribution of the mass ratio  $q$ . The solid black line shows the raw distribution for our sample while the dashed black line shows the distribution adjusted for possible selection bias as described in the text. Also shown is the predicted  $q$  distribution for according to a simulation based on the method of Nie et al. (2012) (blue dot-dash line) and a similar simulation except that a flat initial  $q$  distribution was used (pink dotted line). All distributions are normalized to have the same total number of counts as the raw observed distribution.

Duquennoy & Mayor (1991). We used the fit to the  $q$  distribution given by Duquennoy & Mayor (1991) which is a Gaussian curve with a mean of 0.23 and a dispersion of 0.42 (their Figure 10). A similar simulation was made using a flat main sequence distribution for  $q$ , which Raghavan et al. (2010) suggest as a good approximation to their observed  $q$  distribution for  $0.2 < q < 0.95$ . The distributions resulting from these two simulations are shown in Figure 11 along with our observed distribution of  $q$ .

Our raw distribution of  $q$  values differs significantly from each of the simulations. A KS test gives a probability of less than  $1.6 \times 10^{-6}$  that our raw distribution and the simulated distribution using the main sequence  $q$  distribution of Duquennoy & Mayor (1991) come from the same underlying distribution. Similarly, we find a probability of less than 0.006 that our raw distribution and the simulated distribution using the main sequence  $q$  distribution of Raghavan et al. (2010) come from the same underlying distribution.

Looking at Figure 11, it is clear that our raw and bias-corrected distributions are shifted to higher  $q$  values than predicted by the models which use the input distribution of Duquennoy & Mayor (1991). Our distributions are better aligned with that resulting from use of the distribution of Raghavan et al. (2010). We do not find any evidence for an excess of similar-mass binaries with  $q > 0.95$ , in agreement with the findings of Duquennoy & Mayor (1991) but not with Raghavan et al. (2010) who do find such an excess.

#### 4.4. The eccentricities

In the study of the OGLE II ellipsoidal variables by Soszynski et al. (2004) it was noted that about 10% of ellipsoidal variables had non-sinusoidal light curves.

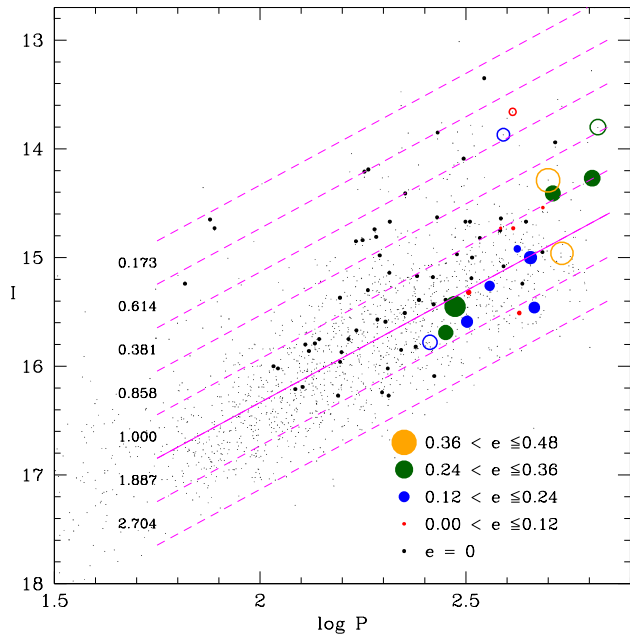


FIG. 12.— The same as Figure 7 except that the colored symbols indicate the value of the eccentricity  $e$ . Open symbols belong to the seven objects studied by Nicholls & Wood (2012).

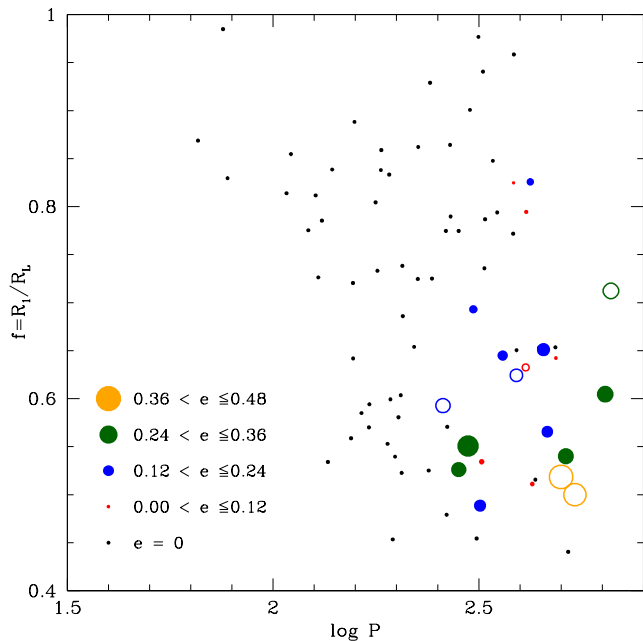


FIG. 13.— Our observed sample of ellipsoidal variables in the  $f$ - $\log P$  plane. The symbols are the same as in Figure 12.

Soszynski et al. (2004) used simple binary light curve models to show that similar light curves could be caused by ellipsoidal variables in eccentric orbits. However, Soszynski et al. (2004) were not able to derive eccentricities as they did not have any radial velocity data and they relied on the light curves alone when deciding if an object had an eccentric orbit. The modelling of both the light and radial velocity curves done by Nicholls & Wood (2012) confirmed that non-sinusoidal light

curve shapes of ellipsoidal variables are indeed caused by eccentric orbits.

If we exclude from our sample the seven objects studied by Nicholls & Wood (2012) which were chosen because they had light curves suggesting eccentric orbits, we find that 15 out of 74, or  $\sim 20\%$  of the systems have eccentric orbits, a higher fraction than estimated by Soszynski et al. (2004). Examination of the list of objects with eccentric orbits given by Soszynski et al. (2004) shows that only 8 of our 16 eccentric objects were considered eccentric by Soszynski et al. (2004). Light and velocity curve modelling, as we have done, clearly reveals more eccentric objects, so the true fraction of eccentric orbits is likely to be roughly 20%, or twice the fraction estimated by Soszynski et al. (2004).

The eccentricities of the objects in our sample are indicated as a function of position on the  $I$ - $\log P$  plane in Figure 12. Because the objects studied by Nicholls & Wood (2012) were deliberately selected to be eccentric, they are shown as open symbols. The objects in Figure 12 which have eccentric orbits (excluding the eccentricity-selected objects of Nicholls & Wood 2012) tend to lie on the fainter, longer period side of the mean  $I$ - $\log P$  relation for ellipsoidal red giant variables. This result can also be seen in Figure 5 of Soszynski et al. (2004). This means that our estimate of 20% for the fraction of ellipsoidal red giant variables that are eccentric may be a lower limit since our sample of objects is biased towards the objects lying above the mean relation in the  $I$ - $\log P$  plane. If we correct for the observational bias to brighter objects using the method applied above for the distributions of  $m_1$  and  $q$ , but using the restricted sample containing objects from Nie & Wood (2014) and Nicholls et al. (2010) only, we estimate that 28% of ellipsoidal variables with  $1.75 < \log(P) < 2.85$  should have eccentric orbits.

The red giant ellipsoidal variables are substantially filling their Roche lobes and these binaries will be subject to tidal forces tending to circularize their orbits. Figure 12 and Figure 5 of Soszynski et al. (2004) show that these ellipsoidal variables only have non-zero eccentricity for orbital periods  $P \gtrsim 200$  days. This is similar to the situation for barium stars (Jorissen et al. 1998) which are binaries that in the past are thought to have substantially filled their Roche lobes and undergone mass transfer by an enhanced stellar wind (e.g. Karakas et al. 2000). However, spectroscopic binaries containing a red giant, but where the Roche lobe is not necessarily substantially filled, show eccentric orbits down to orbital periods of  $\sim 10$  days (Boffin et al. 1993). Those systems presumably lie below the fainter edge of the  $I$ - $\log P$  sequence for ellipsoidal variables in Figure 12. Here, their very low amplitude ellipsoidal variability is not detectable by the OGLE observations.

As noted above, the objects which have eccentric orbits tend to lie on the fainter, longer period side of the mean  $I$ - $\log P$  relation for ellipsoidal red giant variables. The longer periods of these objects at a given  $I$  means that they will tend to have larger orbital separations and hence smaller values of  $R_1/a$  than their shorter period counterparts with circular orbits. Since the tidal circularization time varies as  $(R_1/a)^{-8}$  (e.g. Soker 2000), this means that the systems with longer periods should have longer circularization times and are hence they are more likely to have eccentric orbits, as observed. Note that the Roche lobe filling factor is  $f = R_1/R_L = h(q)R_1/a$  (where  $h(q)$  can be obtained from Equation 5 above), so that binaries with smaller values of  $f$  will have smaller values of  $(R_1/a)$  and hence should have

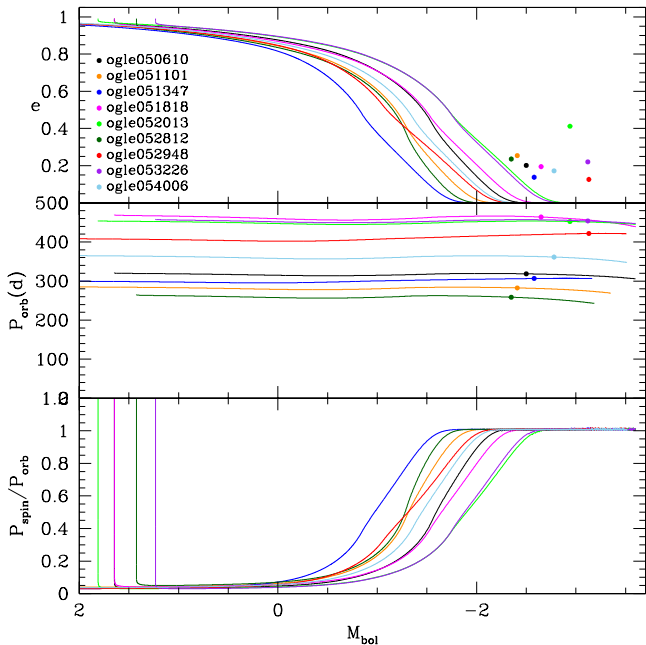


FIG. 14.— The variation of eccentricity, orbital period and the ratio of spin to orbital period for low mass ( $m_1 < 1.85 M_\odot$ ) stars as they evolve up the RGB. Current values of eccentricity and orbital period are shown by dots of different color for nine of our observed systems (we have no rotational velocity measurements so there are no observational points in the bottom panel). The lines show simulations for each of the nine systems, with line color matching the dot color. See text for details.

longer circularization times and be more likely to have eccentric orbits. This is seen to be the case in Figure 13 which shows that in the  $f$ -log  $P$  plane, the detectable ellipsoidal binary systems with eccentric orbits tend to have small  $f$  values, as well as long orbital periods.

## 5. IMPLICATIONS FOR TIDAL INTERACTION THEORIES

We have derived complete orbital solutions for 81 binary systems containing a red giant primary with a luminosity in the upper two magnitudes of the RGB, and 22 of these systems currently have a non-zero eccentricity. Since we know all the properties of this unique set of 22 eccentric binary systems, we can use them to test tidal theories by seeing if these theories allow the observed non-zero eccentricity to exist. To do this, we selected the 9 systems (seven from Nie & Wood 2014 and two from Nicholls & Wood 2012) in our sample that have current eccentricities  $e > 0.1$  and red giant primary masses  $m_1 < 1.85 M_\odot$  so that they are evolving up the low mass RGB. The evolution of these systems was followed using the prescriptions in the standard model of Nie et al. (2012), together with the assumption of non-zero eccentricity. The effects of tides on eccentricity, orbital period and spin period of the red giant are taken into account with the widely-used formulae of Zahn (1977, 1989) and Hut (1981), as implemented in Hurley et al. (2002). Specifically, we use Equations 6, 11, 20, 25, 26 and 30–35 from the latter paper. The calculations were started at the base of the RGB, where it was assumed that the red giant had no spin angular momentum and that the eccentricity was very large (a value of 0.99 was used). This latter assumption was made in order to produce the maximum possible value of  $e$  at all stages of evolution up the RGB. The initial orbital period and masses

were adjusted so that the system had its observed period and derived masses at its current observed red giant luminosity.

The results of these evolution calculations for each of the 9 modelled systems are shown in Figure 14. The base of the giant branch was fainter than the plotted luminosity range except for the four most massive stars which have masses close to  $1.8 M_\odot$  and luminosities  $M_{\text{bol}} \approx 1$  at the base of the giant branch. It can be seen that at low luminosities ( $M_{\text{bol}} \geq 0$ ) the eccentricity is large and has not changed much from the initial value while the spin period is much shorter than the orbital period. This short spin period is a result of the fact that there is strong spin-orbit coupling which has spun up the red giant very quickly (see the rapid decrease in the spin period in the bottom panel of Figure 14 for the 3 most massive stars). This rapid spin up, and the small ratio of  $P_{\text{spin}}/P_{\text{orb}}$ , is due to the high eccentricity which means that the periastron distance is small, and at periastron tidal effects are large and the orbital velocity is high thereby causing the rapid spin up of the red giant. In all cases, as the red giant starts to substantially fill its Roche lobe between  $M_{\text{bol}} = -0.5$  and  $-2.5$ , tides effectively circularize the orbit and the spin and orbital periods equalize. As a result of the latter effect, some spin angular momentum is fed back into the orbit and a small increase in orbital period can be seen.

The most obvious outcome of these calculations is that, in every case, the models predict that the observed systems should have been circularized ( $e = 0$ ) by the time they reached the luminosities they are observed to have today, yet the observed eccentricities are clearly non-zero. Given that the models were started with a very high eccentricity, this suggests that the tidal theories we have used for convective red giant stars greatly overestimate the rate of tidal circularization. Although mechanisms have been proposed that can maintain or boost eccentricity, such as the external disk mechanism (Artymowicz et al. 1991; Waelkens et al. 1996) or mass transfer preferentially at periastron (Soker 2000), these mechanisms would require a substantial amount of circumbinary dust whereas mid-infrared photometry suggests that such circumbinary dust does not exist in these systems (Nicholls et al. 2010). Note that our finding that tidal circularization rates are *overestimated* in red giants is the reverse of the finding for main sequence binaries where it is estimated that the tidal circularization rates are *underestimated* by factors of 50 to 100 (Meibom & Mathieu 2005; Belczynski et al. 2008; Geller et al. 2013). To test how much the tidal circularization rates for binaries with a red giant primary would need to be adjusted to get agreement with observed eccentricities, we follow Belczynski et al. (2008) and introduce a factor  $F_{\text{tid}}$  which multiplies the rates of change of eccentricity and spin due to tides (Equations 25 and 26 of Hurley et al. 2002) and re-run the simulation which was shown in Figure 14. In Figure 15, we show the results for  $F_{\text{tid}} = 0.01$ . This value of  $F_{\text{tid}}$  produces reasonable agreement between the observed and predicted eccentricities, at least when assuming that the initial eccentricity is large. Our estimated value of  $F_{\text{tid}}$  is a factor of  $\sim 10^4$  smaller than the values of 50–100 estimated for main sequence stars by Belczynski et al. (2008) and Geller et al. (2013). It seems that severe modifications of tidal theories in convective stars are required in order to be able to model stars with widely different structures using a single theory.

## 6. SUMMARY AND CONCLUSIONS

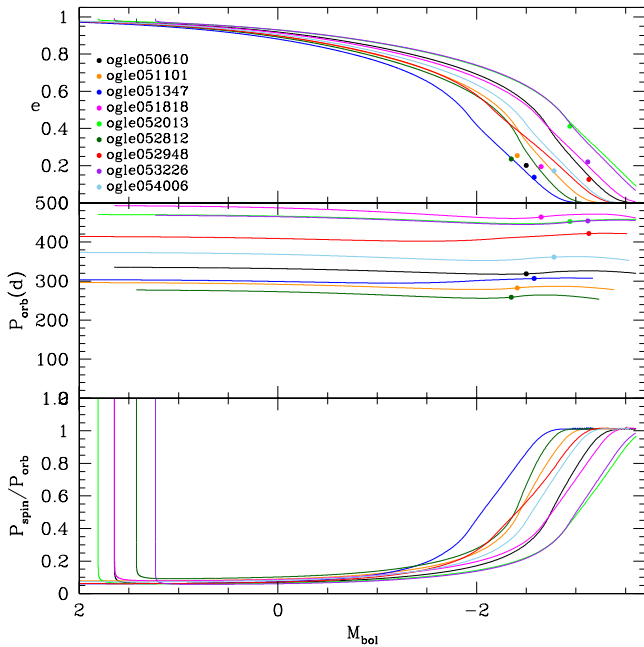


FIG. 15.— The same as Figure 14 but using a tidal damping factor  $F_{\text{tid}} = 0.01$ .

We have carried out orbital modelling for 81 ellipsoidal red giant binaries with the 2010 version of the WD code. The working sample was collected from the works of Nie & Wood (2014), Nicholls et al. (2010) and Nicholls & Wood (2012) and it contains 59 systems with circular orbits and 22 systems with eccentric orbits. Using this sample, and correcting for selection bias, we compare the derived distributions of primary mass  $m_1$  and mass ratio  $q = m_2/m_1$  with model predictions for these distributions based on the methods in Nie et al. (2012). We find values of  $m_1$  from 0.6–9  $M_{\odot}$  and a peak in the distribution of  $m_1$  near 1.5  $M_{\odot}$ , consistent with studies of

the LMC star formation history which show a burst of star formation starting  $\sim 4$  Gyr ago. The derived distribution of  $q$  is in better agreement with the flat  $q$  distribution derived for the solar vicinity by Raghavan et al. (2010) than it is with the solar vicinity  $q$  distribution derived by Duquennoy & Mayor (1991) which favors lower  $q$  values. We found that about 20% of red giant ellipsoidal binaries have eccentric orbits, twice the fraction found by Soszynski et al. (2004) in their OGLE II sample. We also note that half the objects found to have eccentric orbits after modelling the light and velocity curves were not noted by Soszynski et al. (2004) to be eccentric as a result of examination of the light curve alone. The complete parameter sets obtained for the eccentric red giant binary systems were used to test standard theories of tidal interaction in eccentric binaries containing a convective star (Zahn 1977, 1989; Hut 1981). It was found that the tidal circularization rates predicted by these theories are about 100 times *faster* than allowed by the existence of eccentric red giant binaries on the upper parts of the RGB. This contrasts with studies of convective main sequence binaries where the tidal circularization rates predicted by the standard theories are about 50–100 times *slower* than observations suggest. We conclude that current theories of tidal dissipation in convective stars need to be substantially improved.

#### ACKNOWLEDGEMENTS

JDN is supported by the National Natural Science Foundation of China (NSFC) through grant 11303043 and the Young Researcher Grant of National Astronomical Observatories, Chinese Academy of Sciences. PRW was partially supported in this work by the Australian Research Council’s Discovery Projects funding scheme (project number DP120103337). CPN is a Lise Meitner fellow and acknowledges support by the Austrian Science Fund (FWF) under project number M 1696-N27. The authors would like to thank Stephen Justham for useful discussions regarding observational tests of tidal theories. We would also like to thank the referee for helping us improve the presentation of the paper.

#### REFERENCES

- Alencar, S. H. P., & Vaz, L. P. R. 1997, *A&A*, 326, 257  
 Artymowicz, P., Clarke, C. J., Lubow, S. H., & Pringle, J. E. 1991, *ApJ*, 370, L35  
 Belczynski, K., Kalogera, V., Rasio, F. A., et al. 2008, *ApJS*, 174, 223  
 Bertelli, G., Girardi, L., Marigo, P., & Nasi, E. 2008, *A&A*, 484, 815  
 Boffin, H. M. J., Cerf, N., & Paulus, G. 1993, *A&A*, 271, 125  
 Cutri, R. M., Skrutskie, M. F., van Dyk, S., et al. 2003, *VizieR Online Data Catalog*, 2246, 0  
 de Grijs, R., Wicker, J. E., & Bono, G. 2014, *AJ*, 147, 122  
 Dopita M., Hart J., McGregor P., Oates P., Bloxham G., Jones D., 2007, *Ap&SS*, 310, 255  
 Dopita M., et al., 2010, *Ap&SS*, 327, 245  
 Duquennoy A., Mayor M., 1991, *APP*, 248, 485  
 Eggleton P. P., 1983, *ApJ*, 268, 368  
 Fraser, O. J., Hawley, S. L., & Cook, K. H. 2008, *AJ*, 136, 1242  
 Geller, A. M., Hurley, J. R., & Mathieu, R. D. 2013, *AJ*, 145, 8  
 Han, Z., Podsiadlowski, P., & Tout, C. A. 2002, *Exotic Stars as Challenges to Evolution*, 279, 297  
 Haario, H., Saksman, E. & Tamminen, J. 2001, *Bernoulli*, 7(2), 223  
 Haario, H., Laine, M., Mira, A. & Saksman, E. 2006, *Stat Comput*, 16, 339  
 Houdashelt M. L., Bell R. A., Sweigart A. V., Wing R. F., 2000a, *AJ*, 119, 1424  
 Houdashelt M. L., Bell R. A., Sweigart A. V., 2000b, *AJ*, 119, 1448  
 Hurley, J. R., Tout, C. A., & Pols, O. R. 2002, *MNRAS*, 329, 897  
 Hut, P. 1981, *A&A*, 99, 126  
 Ita, Y., Tanabé, T., Matsunaga, N., et al. 2004, *MNRAS*, 353, 705  
 Jorissen, A., Van Eck, S., Mayor, M., & Udry, S. 1998, *A&A*, 332, 877  
 Kallinger, T., Mosser, B., Hekker, S., et al. 2010, *A&A*, 522, A1  
 Karakas, A. I., Tout, C. A., & Lattanzio, J. C. 2000, *MNRAS*, 316, 689  
 Keller, S. C., & Wood, P. R. 2006, *ApJ*, 642, 834  
 Latham, D. W., Stefanik, R. P., Torres, G., et al. 2002, *AJ*, 124, 1144  
 Madore B. F., 1982, *ApJ*, 253, 575  
 Meibom, S., & Mathieu, R. D. 2005, *ApJ*, 620, 970  
 Morris, S. L. 1985, *ApJ*, 295, 143  
 Nicholls, C. P., Wood, P. R., & Cioni, M.-R. L. 2010, *MNRAS*, 405, 1770  
 Nicholls, C. P., & Wood, P. R. 2012, *MNRAS*, 421, 2616  
 Nie, J. D., Wood, P. R., & Nicholls, C. P. 2012, *MNRAS*, 423, 2764  
 Nie, J. D., & Wood, P. R. 2014, *AJ*, 148, 118  
 Pawlak, M., Soszyński, I., Pietrukowicz, P., et al. 2014, *Acta Astron.*, 64, 293  
 Piatti, A. E., & Geisler, D. 2013, *AJ*, 145, 17  
 Raghavan, D., McAlister, H. A., Henry, T. J., et al. 2010, *ApJS*, 190, 1  
 Soker, N. 2000, *A&A*, 357, 557  
 Soszynski, I., Udalski, A., Kubiak, M., et al. 2004, *Acta Astron.*, 54, 347  
 Soszynski, I., Dziembowski, W. A., Udalski, A., et al. 2007, *Acta Astron.*, 57, 201  
 Stello, D., Huber, D., Bedding, T. R., et al. 2013, *ApJ*, 765, L41  
 Szymanski, M. K. 2005, *Acta Astron.*, 55, 43  
 Udalski, A., Kubiak, M., & Szymanski, M. 1997, *Acta Astron.*, 47, 319  
 Waelkens, C., Van Winckel, H., Waters, L. B. F. M., & Bakker, E. J. 1996, *A&A*, 314, L17  
 Wilson R. E., 1979, *ApJ*, 234, 1054  
 Wilson R. E., 1990, *ApJ*, 356, 613  
 Wilson, R. E., & Devinnay, E. J. 1971, *ApJ*, 166, 605  
 Wilson, R. E., Chochol, D., Komžík, R., et al. 2009, *ApJ*, 702, 403  
 Wood, P. R., Alcock, C., Allsman, R. A., et al. 1999, *Asymptotic Giant Branch Stars*, IAUS, 191, 151  
 Wood, P. R. 2000, *PASA*, 17, 18  
 Wood, P. R. 2015, *MNRAS*, 448, 3829  
 Zahn, J.-P. 1977, *A&A*, 57, 383  
 Zahn, J.-P. 1989, *A&A*, 220, 112